## PAPER

Check for updates

# Interface roughness effects and relaxation dynamics of an amorphous semiconductor oxide-based analog resistance switching memory†

G. R. Haripriya, [ID] Hee Yeon Noh, [ID] Chan-Kang Lee, June-Seo Kim, [ID] Myoung-Jae Lee and Hyeon-Jun Lee [ID] *

The analog resistive switching properties of amorphous InGaZnO$_x$ (a-IGZO)-based devices with Al as the top and bottom electrodes and an Al–O$_x$ interface layer inserted on the bottom electrode are presented here. The influence of the electrode deposition rate on the surface roughness was established and proposed as the cause of the observed unusual anomalous switching effects. The DC electrical characterization of the optimized Al/a-IGZO/AlO$_x$/Al devices revealed an analog resistive switching with a satisfactory value for retention levels, but the endurance was found to decrease after 200 cycles. The predominant conduction mechanism in these devices was found to be thermionic emission. An in-depth analysis was performed to explore the relaxation kinetics of the device and it was found that the current has a lower decay rate. The current level stability was tested and found reliable even after 5 h. The cost-effective and precious metal-free nature of the a-IGZO memristor investigated in this study makes it a highly desirable candidate for neuromorphic computing applications.

## Introduction

The advent of neuromorphic computing over von Neumann computation has facilitated efficient high-density data handling, overpowering Moore's law in the memory industry.[1–3] The adaptation of human brain modelling in artificial intelligence (AI) demands new techniques and materials. Memristors, the fourth (or missing) entity of the fundamental pyramid, form the heart and brain of such an AI-based system.[4,5] Owing to their ability to handle massive amounts of data with a very low power consumption at miniaturized dimensions and very high switching frequencies, their use spans an extremely wide spectrum of technological applications.[6–11] This includes pattern recognition, fingerprint encryption, intelligent organs, and space programs.[6–11] The last decade has witnessed an increasing growth of research on memristors, resulting in the development of cost-effective devices with enhanced properties and performances.

Recently, memristors with a-InGaZnO$_x$ (a-IGZO) as the active layer have been attracting considerable attention owing to their efficient resistive switching properties (which can be controlled by the oxygen vacancy composition), low-temperature fabrication conditions, compatibility in cascading with thin film transistors in system-on-panel applications, down scalability as it is devoid of constraints from grain boundaries during size reduction,[12–15] and many other features. Investigations have been conducted to improve a-IGZO-based memristors according to the requirements of the scientific community. The nature of the resistive switching in a-IGZO-based memristors could be effectively tuned by the choice of electrodes, varying layer thicknesses, elemental stoichiometry of the a-IGZO, parametric variation of a-IGZO deposition conditions, proximity of an additional layer, thermal effects, *etc*.[16–25] Earlier work in the literature on Al/a-IGZO/Al memristor devices reported analog/gradual resistive switching (GRS) with negative SET and positive RESET bias conditions.[26] More recently, abrupt/filament-type switching (ARS) with positive SET and negative RESET bias conditions has been reported in contrast to the previous studies.[27] However, the values of voltages and currents involved in the two above-cited reports are comparable where the effect of the interface layer in the oxidized electrode was considered although with different explanations. Most of the reported literature on a-IGZO memristors exhibited abrupt (filament type) resistive switching, whereas mimicking human brain functionalities favours analog/gradual resistive switching.[20,28]

Here, we report on the observation of analog resistance switching behaviour of a noble metal-free a-IGZO-based memristor and discuss the possible reasons behind the anomalous behaviour observed with the same layer structure during the initial development stage. We attempt to correlate the earlier

*Division of Nanotechnology, DGIST, 42988, South Korea.*
*E-mail: dear.hjlee@dgist.ac.kr*

reports with contrasting results by suggesting the role of interface effects in such devices with the experimental outcomes. Also, we present the detailed analog switching aspects of the device with same layer structure but fabricated under optimized conditions to comply with neuromorphic computing applications. Additionally, the transport mechanism is discussed based on the results obtained from cyclic endurance and retention measurements.

## Experimental methods

Amorphous-InGaZnO$_x$ (a-IGZO)-based memristor devices (refer to Fig. 4(a)), used for the study presented here, were fabricated on SiO$_2$(300 nm)/Si wafer. A 100 nm thick aluminium bottom electrode was deposited on 2.5 cm × 2.5 cm pieces of the substrate using shadow mask patterning in commercial electron beam vacuum evaporation equipment (SORONA SRN200). Electrode formation was conducted with a deposition rate ranging from 0.4 to 2.5 Å s$^{-1}$ at a chamber pressure of $\sim$10$^{-6}$ torr. The bottom electrode was then subjected to oxygen plasma treatment under optimized plasma conditions (O$_2$ gas: 10 sccm, 100 W, exposure time: 60 s) to create a thin layer of AlO$_x$ on the bottom electrode using a plasma chamber in the sputtering cluster system (Pure Vacuum Technology). An active a-IGZO layer with a thickness of $\sim$25 nm was then deposited on the Al–O$_x$/Al structure in the presence of oxygen partial pressure (Ar : O$_2$ → 49 : 1 sccm) for the optimized switching conditions using an RF magnetron sputter unit in the same cluster system (200 W, 0.46 Å s$^{-1}$). The top Al electrode ($\sim$100 nm) was then deposited on the a-IGZO layer in the same manner as the bottom electrode.

Cross-sectional analysis of the device's structure and the layer thickness analysis were performed using high resolution transmission electron microscopy (HRTEM) (Themis Z, Thermo Fischer Scientific). The surface roughness of the layer was quantified using atomic force microscopy (AFM, Park Systems) and analysed using the AFM image processing and analysis program in XEI software (Park Systems). All electrical experiments presented in this study were conducted using a Keithley source meter with a probe station and its associated electronics. X-ray photoelectron spectroscopy (XPS, Thermo Scientific ESCALAB 250Xi) was conducted for surface analysis with Ar etching to determine the elemental states in the layers. Devices of 100 × 100 μm$^2$ area with electrodes deposited at 0.8 Å s$^{-1}$ were used for the detailed characterization presented here. Optical observations on the device during the electrical characterization were performed using thermal reflection microscope (TRM250) equipment (Nanoscopesystems).

## Results and discussion

### Surface effects on resistive switching

The preliminary DC electrical characterization studies of the Al/a-IGZO/AlO$_x$/Al device processed with an electrode deposition rate of 1.5 Å s$^{-1}$ are presented in Fig. 1(a), with a few cyclic repetitions in the inset. The observed bipolar resistive switching has abrupt transitions from a high-resistance state (HRS) to a low-resistance state (LRS) marked by a jump at $\sim$2.5 V on the application of a positive bias. A similar jump is noticed at $\sim$−1.8 V, indicating a transition from LRS to HRS during the application of a negative bias. All voltages were applied to the top electrode, whereas the bottom electrode was grounded. However, the observed SET/RESET voltages (associated with the current jumps) were found to be highly unstable over several cycles. The device ended up settling, after 11 cycles, in an unrecoverable read-only/low resistance state (inset of Fig. 1(a)).

The $I$–$V$ characteristics presented in Fig. 1(a) show the behaviour based on abrupt resistance switching, which may be caused by the sporadic formation of conduction filaments inside the sample. The roughness/unevenness of the various layers involved in the memristor stack has been reported to be the origin of abrupt switching in some of the oxide-based memristors. For instance, Nandi et al. (2015)[29] and Charpin-Nicolle et al. (2020)[30] had discussed the investigations on HfO$_x$-based devices with varying roughness by thickness/morphological modifications made on the bottom electrodes to moderate the electric field or forming voltage with the observation of abrupt resistive switching, while Ahn et al. (2018)[31] had discussed the effective control of filament formation by introducing nano pins on a unipolar NiO$_x$ device structure. On the other hand, the observation of abrupt switching due to the highly rough bottom electrode and a dynamic behaviour with a thick layer (80 nm) of the TiO$_x$ active material sandwiched between electrodes of different materials ((Pd and Ti) reported by R. Hu et al. (2021)).[32]

To correlate the effect of the fabrication conditions on layer uniformity and thus resistive switching, we conducted surface roughness measurements through AFM analysis (5 × 5 μm$^2$) for Al thin films with different deposition rates, treated with different oxygen plasma conditions. Fig. 1(b) represents the root mean square (RMS) value of the surface roughness for 100 nm thick Al films deposited with different rates of 0.4, 0.8, 1.5 and 2.5 Å s$^{-1}$. The roughness profiles of the as-deposited films are represented by grey-coloured half-filled squares, while the roughness profiles for thin films treated with oxygen plasma with powers of 50 W and 100 W are represented by half-filled blue circles and pink triangles, respectively. This result indicates a common trend for all plasma powers, where the roughness increases with the electrode deposition rate.

Nevertheless, the oxygen plasma treatment seems to reduce the RMS values for films, which becomes smaller as the plasma power increases. Fig. 1(c) and (e) show the AFM 3 D topography maps of the Al thin films fabricated with deposition rates of 1.5 and 0.8 Å s$^{-1}$, respectively. Fig. 1(d) and (f) show the cross-sectional STEM images of the Al/a-IGZO/AlO$_x$/ Al devices, with Al electrode deposition rates of 1.5 and 0.8 Å s$^{-1}$, respectively. The AFM and cross-sectional STEM measurements clearly identify an enhancement in the sharpness of local needles (peaks) of the Al film surface accompanied by a
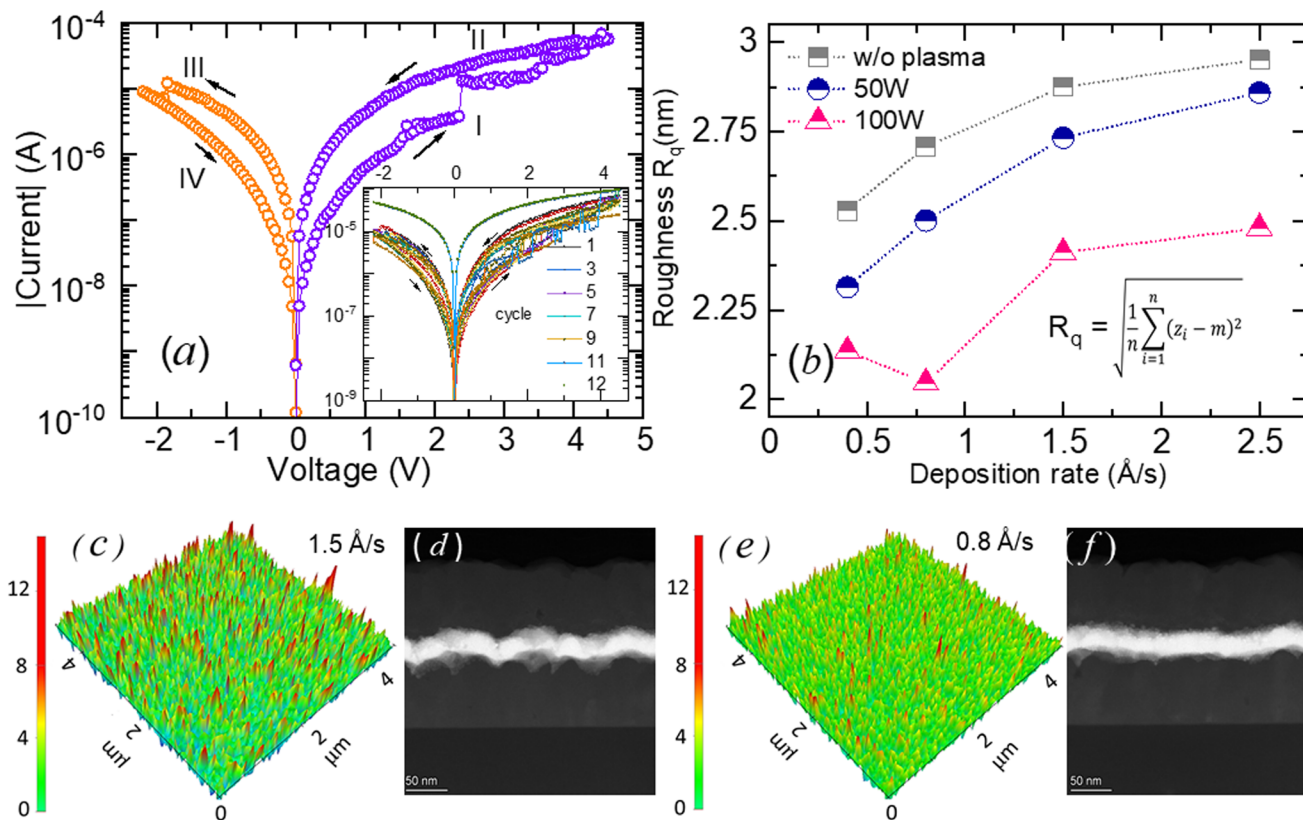
**Fig. 1** (a) Bipolar resistive switching of the Al/a-IGZO/AlO$_x$/Al device with an electrode deposition rate of 1.5 Å s$^{-1}$. The inset represents the cyclic repetition of resistive switching in the same device. (b) Electrode (Al 100 nm) deposition rate *vs.* RMS value of roughness for different plasma powers and AFM images of Al thin films deposited with rates of (c) 1.5 Å s$^{-1}$ and (e) 0.8 Å s$^{-1}$, respectively. (d) and (f) Cross-sectional TEM images of the devices with Al electrodes deposited with rates of 1.5 Å s$^{-1}$ and 0.8 Å s$^{-1}$, respectively, and having bottom electrodes that had undergone oxygen plasma treatment soon after the Al deposition.

degraded flatness of the wide section, leading to an increase in the surface roughness when the layer deposition rate was increased. The non-uniform surface roughness and flatness of the various layers may lead to highly sensitive electrical properties.

Earlier reports have demonstrated that oxygen plasma treatment can be effectively used for the formation of metal–oxide thin films on metal surfaces and for the surface cleaning of metallic thin films, by reducing the surface roughness.[27,33–37] By adjusting the electrode deposition rate and optimizing the oxygen plasma treatment conditions, a drastic change is observed in the electrical characteristics. This is manifested by a gradual variation in the current with the applied bias, possibly owing to the change in the transport mechanism. This will be discussed in detail in later sections.

Fig. 2 shows schematic of the device's cross-section. The Al electrodes are indicated by golden yellow blocks at the top and bottom. The oxygen vacancies, oxygen ions, and bonded oxygen are indicated by red, sandal, and off-white-coloured spheres, respectively. Fig. 2(a) represents the situation when the electrode surfaces are flat, or of negligible roughness, in the absence of an applied bias, while Fig. 2(b) shows the schematic of the device's cross-section with a rough bottom electrode surface under an applied bias. Fig. 2(b) shows the

device's structure for which the bottom electrode was deposited at a rate of 1.5 Å s$^{-1}$ or higher. The influence of the surface roughness on the observed electrical behaviour can be explained as follows. In general, when a potential bias is applied to the electrodes in a sandwich structure with an oxide switching layer, oxygen or oxygen vacancies move under the influence of the electric field formed between the electrodes. The accumulated carriers (oxygen vacancies) generate a change in the resistance of the entire device, leading to current conduction.

In abrupt resistive switching, (as shown in Fig. 1(a)) the oxygen vacancies form linear (conical sometimes) vertical filaments, connecting the top and bottom electrodes. In contrast, a layer-by-layer accumulation of the same occurs in the planar direction in the case of gradual resistive switching (Fig. 5(a)). Due to this phenomenon, the accumulated oxygen or oxygen vacancies form a vertical columnar structure that acts as the conducting path between the electrodes. Additionally, the presence of needle-like points on the bottom electrode shortens the distance to the top electrode, leading to a faster movement of the carriers compared to the remaining surface. Hence, the devices with a bottom layer deposited at a higher deposition rate (*i.e.*, with higher surface roughness) exhibit an abrupt/conduction filament-type resistive switching due to the generation
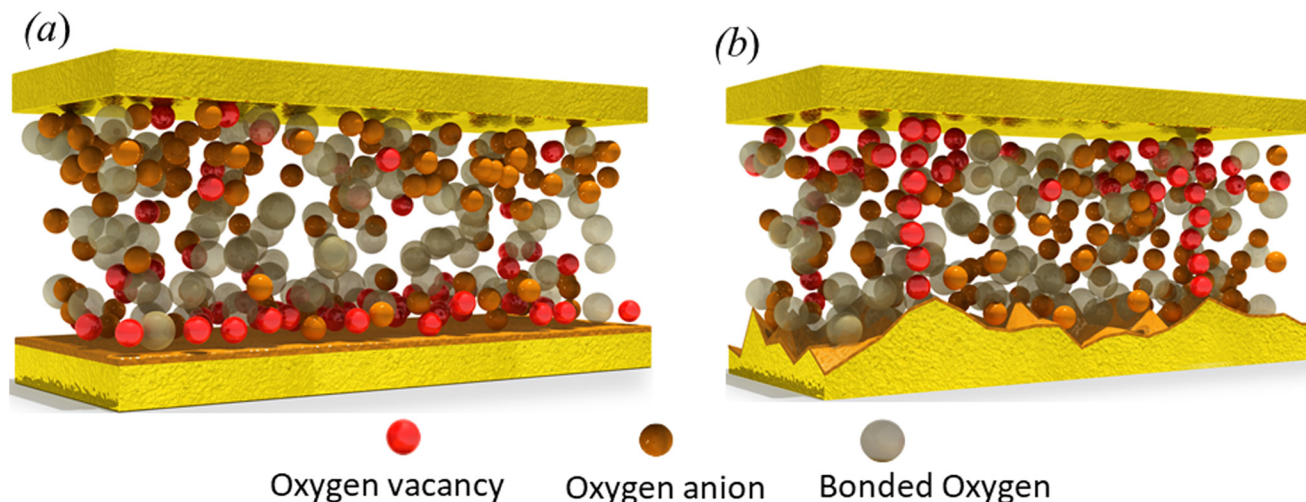
**Fig. 2** Artistic representation of the device cross-section: (a) in the absence of an applied bias with smooth interfaces at each layer and (b) eventual occurrence of oxygen vacancy filament formation (red spheres) originated from the peaked locations (needle points) due to bottom electrode roughness. Golden yellow blocks on the top and bottom represent Al electrodes, (off-white spheres represent oxygen bonded to IGZO molecules), sandal-coloured spheres represent oxygen ions and red spheres represent oxygen vacancies.

of localized filaments. It follows that, based on this model, contradictory results in electrical characteristics could be observed for the same device structure as in previously reported studies, depending on the relative roughness of the electrode and the a-IGZO interface.[26,27,38]

Furthermore, to achieve stable non-volatile resistive switching, the modification of several fabrication parameters, namely layer thicknesses, deposition rates, plasma parameters for oxygen plasma treatment, and the oxygen partial pressure ratio to Ar for a-IGZO deposition, were considered. The device processed with an electrode deposition rate of 0.8 Å s$^{-1}$ was found to exhibit a gradual resistance change with the applied bias and was used for further investigations presented in this paper.

In order to confirm the observed abrupt and gradual resistive switching behaviours in the devices, differed only by electrode deposition rates, area dependence on the current was experimented. Fig. 3(a) and (b) represent the variation of current measured at 0.5 V for devices with different device areas of $50 \times 50$, $100 \times 100$, $150 \times 150$ and $200 \times 200$ $\mu m^2$ for the two deposition rates of 1.5 Å s$^{-1}$ (Fig. 3(a)) and 0.8 Å s$^{-1}$ (Fig. 3(b)), respectively. A linear increment of current with the device area in Fig. 3(b) indicates that the devices processed with 0.8 Å s$^{-1}$ exhibit gradual/analog resistive switching while the devices with 1.5 Å s$^{-1}$ show nonlinear area dependence. The device structure used for the study is schematically presented in Fig. 3(c). The representation is made with the circular area for better perception, while real experiments were conducted with a rectangular/square device area.

### Structural aspects

The material stability, layer-by-layer structure and chemical composition of the device under investigation (processed with an electrode deposition rate of 0.8 Å s$^{-1}$) were tested using high-angle annular dark-field scanning transmission electron microscopy (HAADF-STEM) measurements of the device's cross-section and X-ray photoelectron spectroscopy (XPS) with Ar etching. The extracted key points are indicated in different sections of Fig. 4. A schematic of the fabricated crossbar structure is shown in Fig. 4(a), along with the proposed layer-by-layer structure and cross-sectional HAADF image. Fig. 4(b) shows that the oxygen concentration at the a-IGZO/Al bottom interface (at the 60 nm position) is higher than that at the Al/a-IGZO top interface. Correlating the depth profile (line) from the cross-sectional STEM analysis (Fig. 4(b)) with the XPS spectra obtained with Ar etching, the a-IGZO/Al interface is found to have oxidized Al (designated as AlO$_x$, with a thickness of ~10 nm), originating from the oxygen plasma treatment as well as the proximity to a-IGZO. To confirm the oxidation state of oxygen near the a-IGZO/Al bottom electrode (BE) interface, the analysis was performed by dividing it into two regions (i.e., I and II in Fig. 4(b)) based on the proximity to a-IGZO and Al. In Fig. 4(b), region I is the a-IGZO/Al interface close to the IGZO layer, and region II is the interface close to the Al bottom electrode.

The XPS spectra of O 1s and Al 2p, taken in the two regions, are presented in Fig. 4(c–f). The O 1s spectra of both regions (Fig. 4(c) and (e)) were deconvoluted into three Gaussian peaks of suitable full width at half maximum (FWHM) for each peak position, which correspond to the metal-bound oxygen (M–O: In/Ga/Zn/Al–O) centred at around ~530–531 eV, the oxygen vacancy (V$_O$) centred at around ~531–532 eV and the loosely bound oxygen (M : OH or O$_{Ads}$) at around ~532–533 eV.[25,39–43] Compared to region I, the proportion of V$_O$ states is relatively larger in region II. In addition, a slight decrease in the M–O peak is observed in region II due to the diminishing/absence of IGZO in this region. In region I, the major contribution to the M–O bond is from IGZO(In/Ga/Zn–O), while in region II
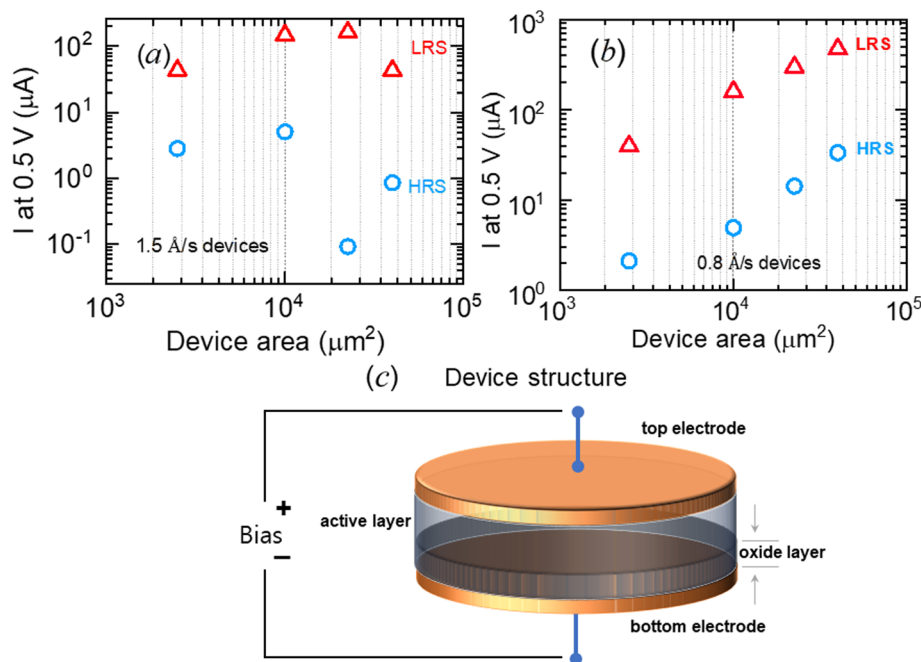
**Fig. 3** Area dependence of the device current at HRS (blue-coloured open circles) and LRS (red-coloured open triangles) measured at 0.5 V on the Al/a-IGZO/AlO$_x$/Al devices with different device areas (50 × 50, 100 × 100, 150 × 150, and 200 × 200 µm$^2$) processed with electrode deposition rates of (a) 1.5 Å s$^{-1}$ and (b) 0.8 Å s$^{-1}$. (c) Schematic of the device structure used for the study, circular geometry is drawn for better perception.

the M–O peak has the major contribution from Al–O. The Al 2p spectra of regions I and II are presented in Fig. 4(d) and (f), exhibiting binary peaks in which the lower energy peak stems from metallic contribution (Al$^0$) and the higher energy peaks originate from the addition of oxide/hydroxyl ligands.[44–48]

A careful deconvolution of the Al 2p spectra resulted in two peaks in region I, and three peaks in region II. The de-convoluted peaks in region I centred at ~72–73 eV and ~75–76 eV are attributed to metallic Al and the binary oxide of Al which is Al$_2$O$_3$, respectively.[44,46,47] In region II, the de-convoluted peaks were found centred at around ~72–73 eV, ~73–74 eV and ~75–76 eV. While the first and third peaks are similar to those in region I, the middle (second) peak appearing on the spectrum in region II corresponds to the presence of AlO$_x$ sub-oxides at the bottom electrode.[45,48] The change in the intensities of the low-energy peaks in both regions indicates a variation in the metallic Al concentration at the interface.

### Analog resistive switching

Electrical (*I–V*) measurements were carried out on the Al/a-IGZO/Al–O$_x$/Al samples, which were manufactured with Al electrodes deposited at 0.8 Å s$^{-1}$, which is the optimized deposition rate. Bias voltages were applied to the top electrode keeping the bottom electrode grounded, as in the previous case. The underlying transport mechanism is also discussed in this section with the help of electrical measurements referring to the existing literature.[21,27,49]

Fig. 5(a) shows the DC current–voltage behaviour of the Al/a-IGZO/Al–O$_x$/Al device with a semi-log plot having voltage on the abscissa and the absolute value of the current on the ordinate. The device exhibits a bipolar gradual resistive switching (analog type) with the end voltages of ~4.5 V for the HRS to LRS (SET) transition and ~−2.2 V for the HRS to LRS (RESET) transition. To confirm the presence of gradual resistance switching in our device, the area dependency of the current for the device structure was tested and the results are presented in Fig. 3.

Few studies in the literature have reported on the analog switching (gradual resistive switching) in a-IGZO-based memristors, which is favourable for AI-related applications (refer to Table 1).[17,20,21,26,49–56] It is found that an analog/gradual resistive switching is observed at the cost of slightly higher values of bias voltages in comparison with the filament-based switching devices. From an application point of view, endurance and retention are two main key parameters in memristors. Nonetheless, they have rarely been mentioned in the literature for the gradual resistive switching type, as shown in Table 1.

The inset of Fig. 5(a) shows the cyclic endurance of the Al/a-IGZO/Al–O$_x$/Al device, and its retention is presented in Fig. 5(i). The results show that the level stability of the device measured over 5 h is highly reliable. The endurance of the device was tested for over 500 cycles, and it was noted that the hysteresis in the current significantly decreased after ~200 cycles with a gradual shifting of the HRS toward LRS. The cumulative distribution of the current read at 0.5 V for HRS and LRS over 500 cycles is shown in the inset of 5(a). To understand the switching/conduction mechanism and the reason for hysteresis degradation, slope analysis was performed on
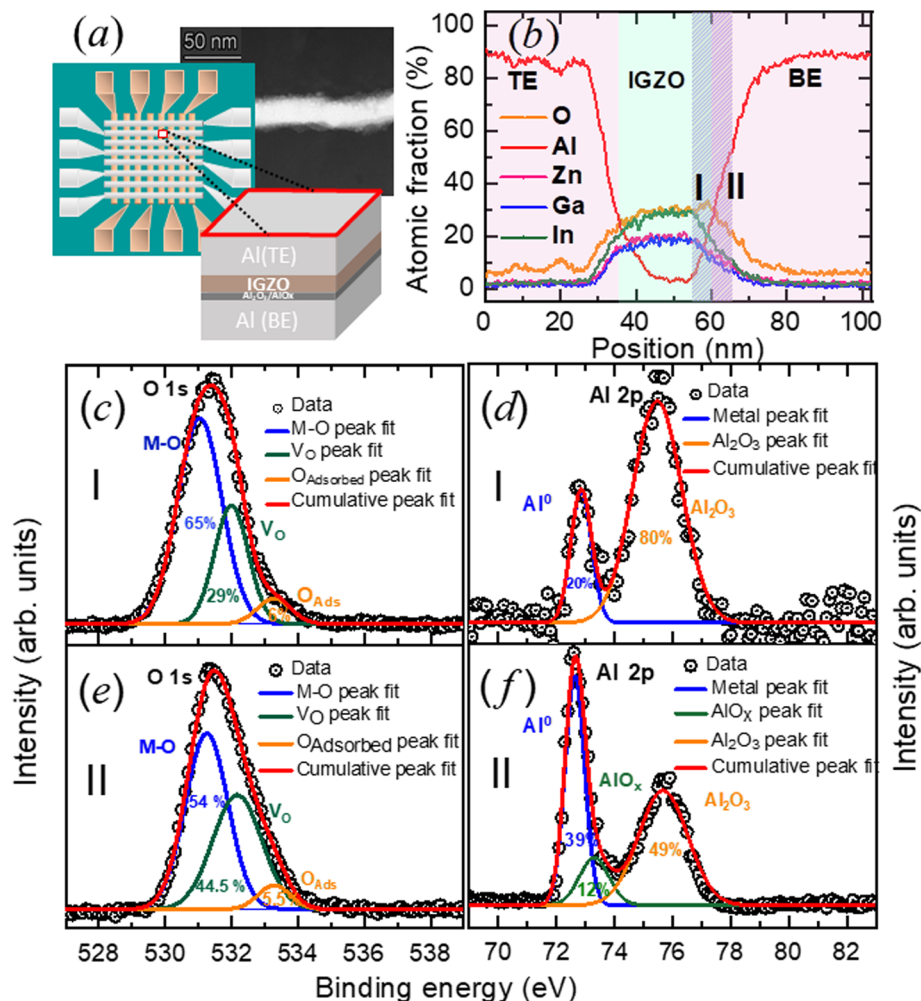
**Fig. 4** (a) Schematic of the crossbar geometry of the device with the corresponding HAADIF image, (b) atomic fraction of the elemental composition of the device from EDS analysis where TE and BE represent the top and bottom electrodes, respectively. Deconvoluted XPS spectra of (c) O 1s near the a-IGZO/Al interface in region I, (d) Al 2p near the a-IGZO/Al interface in region I, (e) O 1s near the a-IGZO/Al interface in region II, and (f) Al 2p near the a-IGZO/Al interface in region II.

the first and 500th cycles of the DC $I$–$V$ curves. The complete SET/RESET loops presented in Fig. 5(a) belong to the first entity of cyclic measurements.

For convenience, we divided a single complete cycle into four cases as follows: the variation of the positive bias in the forward direction (0 V to 4.5 V) is denoted as case I, while the reverse direction (4.5 V to 0 V) is denoted as case II. Similarly, in the negative bias, the forward direction (0 V to −2.2 V) is denoted as case III, while the reverse direction (−2.2 V to 0 V) is denoted as case IV. Fig. 5(b) and (d) show the plots of the above-mentioned cases for the first cycle with the logarithmic values of voltage and current on the abscissa and ordinate, respectively. Fig. 5(c) and (e) represent the same for the 500th cycle. For, the reader's convenience, the corresponding linear voltage values are indicated at the top axes of Fig. 5(b) and (d). The influence of applied bias at the top electrode on the current and barrier potential was investigated and the results are presented in Fig. 5(f–h). Fig. 5(i) shows the multilevel retention characteristics of the current in the HRS and mul-

tiple LRS levels obtained by controlling the end value of applied bias.

The conduction mechanism of such a M/O/M sandwich structure depends on numerous factors consisting of electrode-influenced properties such as the nature of electrodes, the nature of the interface between the electrode and the active layer, and bulk-dependent properties such as trap distribution, mobility, the trap state, the trap density of the active layer, etc.[54,57]

However, the oxygen vacancies in the active oxide layer as well as the active layer–electrode interface are also found to be leading to resistive switching.[26,54,57] The current–voltage characteristics of most a-IGZO-based memristors can be majorly associated with ohmic conduction ($I \approx aV$), space-charge-limited current conduction (SCLC) ($I \approx aV + bV^2$), Child's square law region ($I \approx cV^2$), trap-assisted (filled/unfilled) conduction/tunnelling (TAT), Poole–Frenkel emission (PF) ($\ln(I/V) \propto V^{1/2}$), Fowler–Nordheim tunnelling (FN) ($\ln(I/V^2) \propto V^{-1}$), the thermionic emission model ($\ln(I \propto \sqrt{V})$),[14,15,18,20,21,27,49,54,57] and many more.
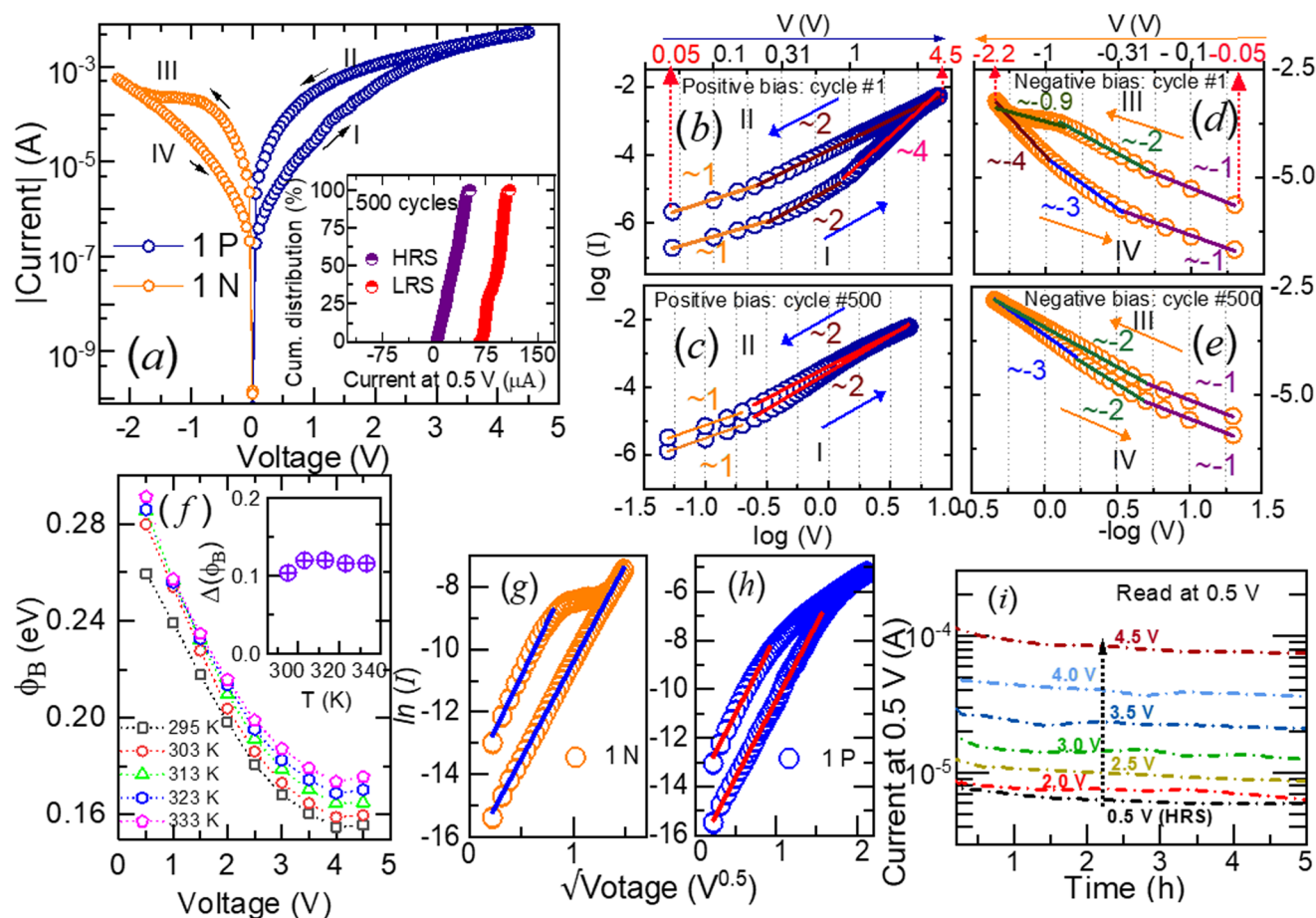
**Fig. 5** Resistive switching behaviour of the fabricated device. (a) Gradual bipolar resistive switching. Blue open circles represent the current during the positive bias on the top electrode (cases I and II) and orange open circles represent the current during the negative bias (cases III and IV). The inset shows the endurance of the device over 500 continuous cycles. (b)–(e) Log $I$ vs. log $V$ plot for the first and 500th cycles with the slope values indicated close to the plot, line indicators are guide to the eyes; (f) variation of $\Phi_B$ with bias voltage for temperatures of 295, 303, 313, 323, and 333 K and the inset shows the invariability of $\Delta\Phi_B$ with temperature; (g) and (h) ln($I$) vs. $\sqrt{V}$ for the negative and positive biases at 295 K, respectively, with lines for guide to the eyes; and (i) multilevel retention of the device for 5 h (18 000 s).

**Table 1** Gradual resistive switching properties of a-IGZO-based memristors from the literature

| Device structure | Voltage limits (SET/RESET) | Endurance [cycles] | Retention (time, s /% remembrance) | Ref. |
|---|---|---|---|---|
| Mo/Al$_2$O$_3$/IGZO/Pd | +8 V/−6 V | 500 | 25/NM | 17 |
| Mo/IGZO/MoOx/Mo | −3 V/+3 V | NM | 640/17 | 20 |
| Au/Ti/IGZO/SiO$_2$/p+-Si | +6 V/−2 V | NM | NM | 21 |
| Al/IGZO/Al | −5 V/+5 V | 100 | NM | 26 |
| Cu/IGZO/p+-Si | +5 V/−4 V | NM | NM | 49 |
| Pd/IGZO/SiO$_2$/p+-Si | +6 V/−4 V | NM | NM | 50 |
| Mo/a-IGZO/Ti/Mo | −4 V/+3 V | NM | NM | 51 |
| Mo/Ti/IGZO/Mo | −2 V/+2 V | NM | NM | 52 |
| Pd/IGZO/SiO$_2$/p+-Si | +6 V/−4 V | 500 | NM | 53 |
| Au/Ti/IGZO/Mo | −3 V/+3 V | 100 | NM | 55 |
| Pt/IGZO$_x$/IGZO$_y$/Pt | +6 V/−6 V | NM | NM | 56 |
| Pd/IGZO/SiO$_2$/p+-Si | +7 V/−3 V | 4 × 10$^4$ | ~100/NM | 54 |

NM: not mentioned in the original source.

Fig. 5(b) and (c) show a drastic variation in the slope values above a bias voltage of ~0.75 V for the 1$^{st}$ and 500$^{th}$ cycles in case I. However, case II exhibits almost the same trend in both cycles. During the negative bias, as shown in Fig. 5(d) and (e), in case III, both cycles exhibited notable variation at higher values, whereas in case IV, the variation was found to be negligible. The close correlation between the slope values extracted from the electrical characterization data and the underlying

transport mechanism can be established by revisiting the literature as discussed later in this section. As shown in Fig. 5(a) and (b), ohmic conduction is inferred for the initial onset of applied bias up to 0.75 V, as indicated by the slope value of 1 for the device under study. At a lower bias, the number of carriers participate in conduction will be lower, resulting in a small but linear increase in the current with the applied bias. As the bias is further increased the main transport mechanism is found to be non-ohmic, reflecting the higher value of the slope in the I–V curve.

In general, the current conduction in a-IGZO active-layer devices is highly influenced by the defects present in the material. Oxygen vacancies and metal ion interstitials, the mostly found defects in a-IGZO, have been reported to play a key role in resistance switching for most devices.[14,23,27,49,55,56,58] The oxygen vacancy states found in a-IGZO are commonly represented as $V_O$, the neutral vacancies which belong to the deep levels; $V_O^+$, the single ionized states $(V_O - \bar{e} \rightarrow V_O^+)$; and $V_O^{++}$, the doubly ionized trap states $(V_O - 2\bar{e} \rightarrow V_O^{++})$, the ionized shallow levels.[53,56,59,60] The sub-gap density of states of a-IGZO with mentions to trap states is presented in Fig. 6(a) for reference.[58,59,61] As indicated in Fig. 6,

shallow levels are easily available for conduction, whereas deep levels become involved only at higher applied biases. The two main types of metal-linked oxygen vacancy sites commonly observed in a-IGZO are graphically presented in Fig. 6(b). The shallow donor states at the top of Fig. 6(b) are found at the sites where edge/face-shared In/Ga–O octahedra and Zn–O tetrahedra are available.[56,60,62,63] Deep/shallow traps are formed at sites where corner-shared $(ZnO)_x$ tetrahedra are available.[56,60,62,63]

In the majority of the gradual switching cases, the involvement of Schottky barrier modulation is non-negligible.[20,26,53] In our devices, a thin $AlO_x$ layer is present in between the bottom Al electrode and the a-IGZO active layer, which could act as a Schottky barrier and get modulated during the application of voltage bias. The effect of the interface layer during switching has been tested using the thermionic emission model,[14,15,18,20,21,27,49,54,57] which can be simply performed by plotting $\ln(I)$ against $V^{0.5}$. Fig. 5(g) and (h) represent the $\ln(I)$ vs. $V^{0.5}$ plot for the negative and positive bias conditions, respectively, at room temperature, RT (295 K). The plot infers that irrespective of the bias polarity, the current conduction follows the thermionic emission model and electron trapping
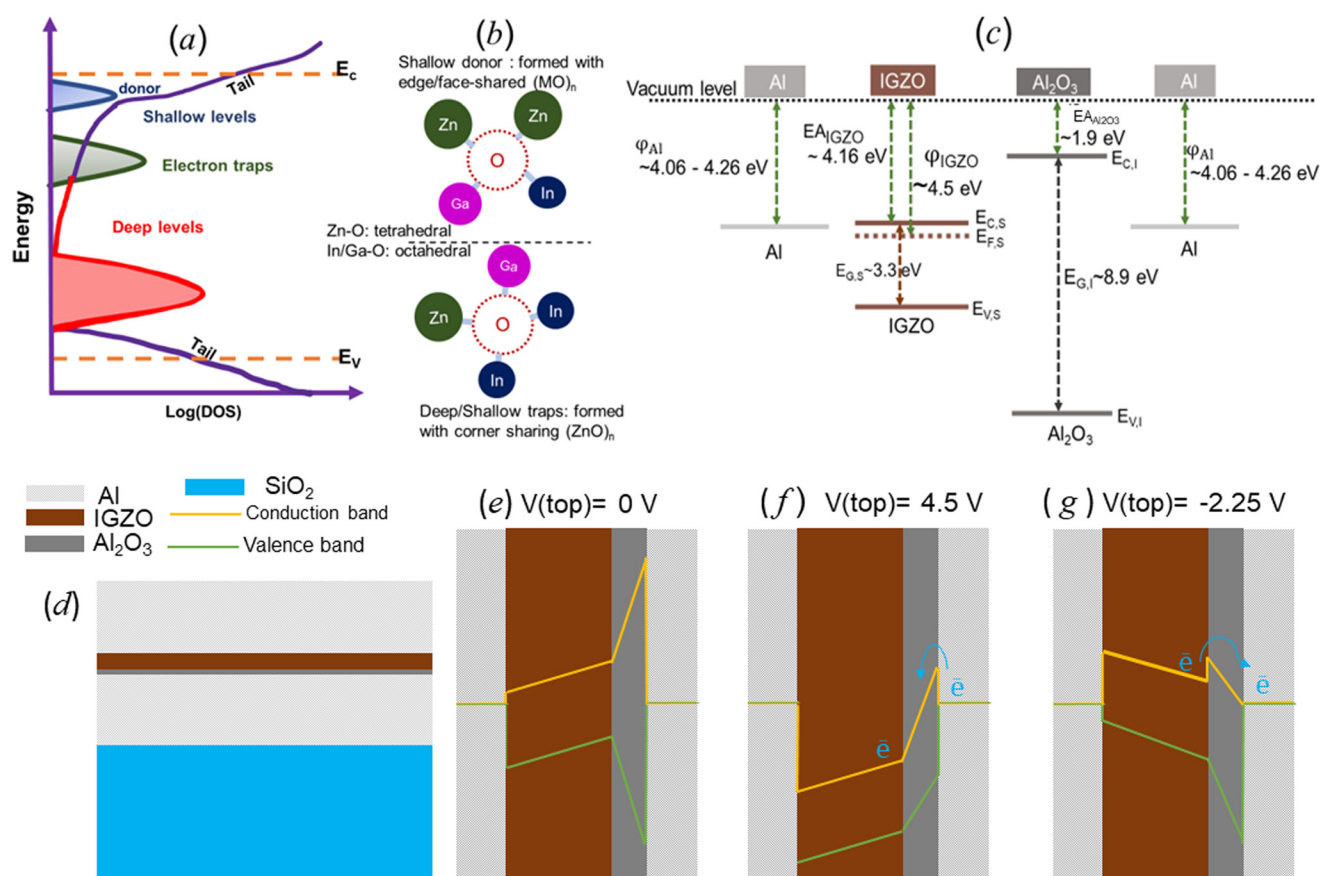


Fig. 6 (a) Pictorial representation of the sub-gap DOS of a-IGZO,[58,59,61] (b) metal-linked oxygen vacancy states in a-IGZO,[55,60,62,63] (c) representation of the work function of different layers (when not in contact) of the device with reference to the vacuum level,[23,24,27,41,49,64,65] and (d) cross-sectional representation of the device structure. Schematic of a flat band representation of the device for the applied bias voltages of (e) 0 V, (f) 4.5 V (SET conditions) and (g) −2.25 V (RESET conditions).

at the a-IGZO/Al interface layer where $AlO_x$ vacant sites are present. The influence of applied bias voltage on the barrier height $\Phi_B$ can be determined with the help of eqn (1),

$$\ln(I/V) = \Phi_B(q/kT) \qquad (1)$$

where $I$ is the memristor current, $V$ is the voltage bias applied on the top electrode, $\Phi_B$ is the Schottky barrier height, $k$ is the Boltzmann constant and $T$ is the absolute temperature.

The Fig. 5(f) describes the variation of $\Phi_B$ with applied bias at different temperatures. During the application of applied bias, $\Phi_B$ is found to decrease from 0.26 eV to 0.15 eV, making the device conductive so that the current value changes from HRS to LRS gradually. When the temperature is increased above RT, 295 K, $\Phi_B$ exhibited the same trend with slightly elevated values. However, the difference in $\Phi_B$ is found to be almost constant with temperature (refer to the inset of Fig. 5(f)) (further explanation is provided in the ESI†).

Fig. 6(c) shows the work function values ($\Phi_{material}$) of the materials forming different layers: Al, a-IGZO and $AlO_x/Al_2O_3$. An ohmic contact is expected for the Al/IGZO junction as $\Phi_{Al} \lesssim EA_{IGZO}$ (electron affinity of IGZO) and the IGZO/$Al_2O_3$ junction as $EA_{Al_2O_3} \ll EA_{IGZO}$, and a Schottky-like contact near the $Al_2O_3$/Al region is expected, according to the band theory of solids.[24,41,64–66] However, the XPS data point towards the presence of $AlO_x$–oxygen vacant sites near to the Al/$Al_2O_3$ interface (refer to Fig. 4). Fig. 6(c) has been drawn with reference to the vacuum level considering that layer materials are independent and are not in proximity to each other. The bottom interface of the a-IGZO active layer and the tunnel layer $Al_2O_3/AlO_x$ in our device was found to have an abundance of oxygen vacancies that are distributed in various energy sublevels, as indicated in Fig. 6(b). However, in the case of the 500th cycle, apart from the slope mismatch in Fig. 5(b) with (c) and Fig. 5(d) with 5(e), uplifting of the hysteresis loop is observed with diminished hysteresis.

The flat-band representations of the device levels with different bias conditions are shown in Fig. 6(e) and (f). The application of a high positive bias at the top electrode gives rise to the lowering of the Schottky barrier aiding the device to settle into the low resistance state while the application of a negative bias will modify the band picture and the electrons are trapped back to their initial positions leaving the oxygen vacancies neutralized, resulting in RESET of the device to its high resistance state.

In a nutshell, during low bias voltages the electron migration is restricted due to the presence of a Schottky barrier at the BE interface. As the voltage is increased ionization of oxygen vacancies takes place, which leads to the generation of electrons as well. The coulombic field created by the ionized carriers leads to the reduction of the Schottky barrier height, aiding the migration of electrons across the barrier during the SET process. When a negative bias is applied on the top electrode keeping the bottom electrode grounded, the neutralization of oxygen vacancies takes place leading to the vanishing of the coulombic field, yielding the restoration of

the Schottky barrier level to its original position causing a hurdle for the electrons to cross the barrier. Hence, during the RESET process, the current is decreased from LRS to HRS. Considering the DC cyclic conditions in which the bias voltage cycles for SET and RESET processes is multiply repeated (here it is 500 cycles), not all the ionized oxygen vacancies were neutralized during the negative bias, causing shrinkage in the hysteresis area.

Confirmation of the exact contribution of the transport mechanism leading to the memristive properties will be elucidated by further investigations. Also, the longevity of the cyclic endurance of our device will be ensured in the near future by means of optimization of the $AlO_x$ layer and bandgap modification of the a-IGZO layer.

### Memory retention

Memristors are often used as artificial synapses in hardware-based neuromorphic computing owing to their functional similarities with the synapses, which provide a linkage among the neighbouring neurons in the biological nervous system.[4,6–9,11,26,27,67] Mostly, the learning and forgetting abilities of the human brain have been utilized as criteria for testing the potential of candidate memristor devices for AI-related applications.[3,7,9,20,28,49,67–70] The stretched exponential function (SEF), given in eqn (2), is the simplest, most adequate, and widely used tool for this purpose.[20,54,68–71]

$$\varphi_t = I_0 \exp\{-(t/\tau)^\beta\} \qquad (2)$$

where $I_0$ is the pre-factor, $\varphi_t$ is the relaxation function, $\beta$ is the stretch index ($0 \leq \beta \leq 1$), and $\tau$ is the characteristic relaxation time. A careful understanding of the SEF reveals that when $t < \tau$, an abrupt drop of $I_0$ occurs, followed by a much slower decay when $t > \tau$, which resembles the human memory behaviour, so that the function is frequently used for memristor decay quantification.[20,69,70] The relaxation/retention loss behaviour of the device was quantified by fitting the SEF as given in eqn (2). In our fit, $I_0$ and $\varphi_t$ are the normalized values of the current read at 0.5 V, right after performing the SET operation at 4.5 V and relaxing over a time $t$ (5 h), respectively. Parameters $\beta$ and $\tau$ can reveal the collective behaviour of all available relaxations related to oxygen vacancies in a-IGZO-based memristors.[20]

The relaxation data for our device were collected as follows (refer to Fig. 7(a)). The first trial was conducted on the device in the DC mode of SET at 4.5 V with a voltage sweep rate of 0.5 V s$^{-1}$. As soon as the voltage reached 4.5 V, the bias was removed, and the current was measured continuously for 5 h with logarithmic intervals of time. The overall behaviour exhibited by the relaxation plot was found to be similar to that of the human brain. The initial decay related to short-term plasticity (STP) is faster than the subsequent decay.[20,68–70] In the case of the human brain, the short-term memory referred to a small amount of information which holds for a short period of time, typically not more than 30 s so that if the holding period is >30 s, it would be under long-term memory.[20] However, the significant initial decay in our device
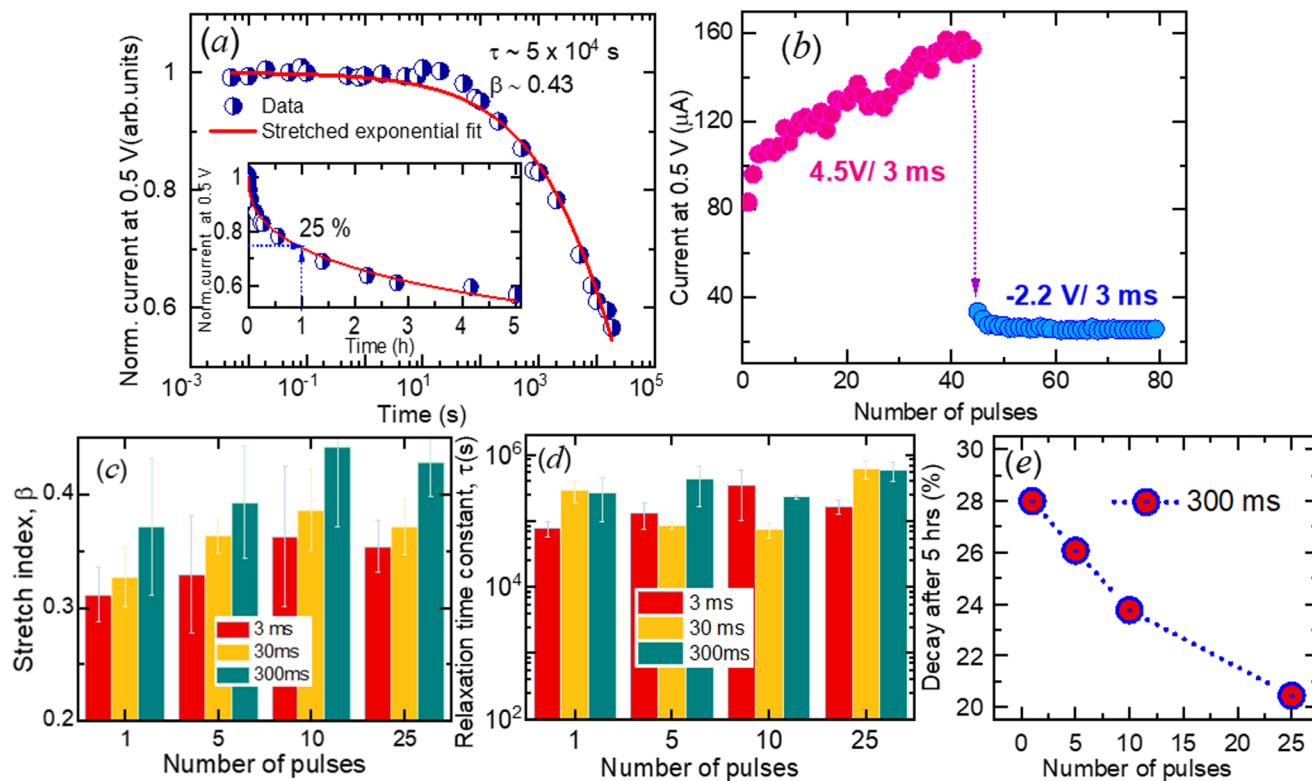
**Fig. 7** (a) Relaxation with DC SET voltage, (b) potentiation and rapid depression for 3 ms pulses, (c) value of the stretch exponent $\beta$, for relaxation, stimulated with various numbers of pulses for different pulse widths, (d) relaxation time constant, $\tau$ vs. the number of stimulating pulses for different pulse widths, and (e) percentage of decay (forgetting) of current during relaxation when prior stimulations carried out with various numbers of pulses for a pulse width of 300 ms.

appears to be more than 30 s, which is much longer than the STP limit.

The stretch index was found to have a value of approximately ~0.43, which is in good agreement with the literature for a-IGZO based devices.[20] However, only ~25% of the initial current was decayed after 1 h of relaxation after the application of the pulse train, which is small compared to many of the earlier reports on a-IGZO-based memristors.[20,69] The relaxation time constant has a value of ~5 × 10⁴ s, which indicates the potential application of the device as a functional entity in memory or storage applications. The value of the relaxation time constant for the trials with a lower number of stimulating pulses (a single pulse) was found to be similar to that of the DC stimulation case (refer to Fig. 7(a) and (d)).

Fig. 7(b) shows the pulsed response of the Al/a-IGZO/AlO$_x$/Al device for a pulse width of 3 ms. Potentiation was conducted with an amplitude of 4.5 V for ~40 positive pulses, and depression was conducted with an amplitude of 2.2 V for ~40 negative pulses. In the potentiation process, the current exhibited a linear response with an increase in the pulse number, and the degree of linearity was found to be ~50%. In contrast, the depression showed an abrupt drop in the current value. The device immediately jumps down to depression from potentiation, which is more rapid than its natural relaxation, upon the application of a negative bias. It seems that the

immediate drop originated from the rapid relaxation of the carriers upon the application of the negative bias, as observed in some of the a-IGZO-based devices.[69]

The effects of pulsed stimulation on relaxation dynamics are summarized in Fig. 7(a), (c) and (d). Relaxation measurements were performed after the stimulation of the device with pulses of different widths (i.e., 3, 30 and 300 ms) and different number of pulses (i.e., 1, 5, 10, and 25 times) for each pulse width. The value of the stretch exponent increases with an increase in the number of pulses, whereas the relaxation time constant lies within the range of 10⁴–10⁵ s for each pulse width. This indicates a change in relaxation dynamics with an increased number of pulses and the extent of stimulation (i.e., pulse width). To verify the nature of the decay, a plot was constructed for the decay percentage of the current at 5 h after pulsed stimulation for 300 ms pulses with a set of pulse numbers, as shown in Fig. 7(e). It was found that the decay percentage is reduced with the number of pulses used for stimulation, which resembles the learning and forgetting patterns of the human brain.[20,68,69]

## Conclusions

The electrical properties generated by the field-induced movement of ionized oxygen vacancies/electrons and their inter-

action with the associated atoms in the active material play a critical role in resistance-based neuromorphic devices which are implemented by mimicking the operational functionalities of the human brain and the nervous system. In this study, an analog resistive switching a-IGZO active layer memristor was established by carefully controlling the electrode deposition parameters. The abnormalities observed in the electrical characteristics were resolved and explained by correlating the surface roughness with the electrode deposition rate. The major transport mechanism was found to be thermionic emission irrespective of the bias polarity, which occurred due to the presence of a thin $AlO_x$ layer, which served as a Schottky barrier, positioned at the a-IGZO/Al bottom interface. The degradation of the hysteresis in the current over cycles was also explained based on the slope analysis as the incomplete neutralization of the ionized oxygen vacancies during the negative bias due to microstructural modifications owing to the continuous application of the electric field to the device. This study is expected to enhance the in-depth understanding of the operating principle of amorphous oxide-based neuromorphic devices and the realization of devices with a high level of reliability during application.

## Author contributions

The manuscript was written through contributions of all authors. All authors have given approval to the final version of the manuscript.

## Conflicts of interest

There are no conflicts to declare.

## Acknowledgements

## References

1 G. E. Moore, *Electronics*, 1965, **38**, 114–117.
2 C. A. Mead, *Nat. Electron.*, 2020, **3**, 434–435.
3 C. A. Mead, *Proc. IEEE*, 1990, **78**, 1629–1636.
4 D. B. Strukov, G. S. Snider, D. R. Stewart and R. S. Williams, *Nature*, 2008, **453**, 80–83.
5 L. O. Chua, *IEEE Trans. Circuit Theory*, 1971, **18**, 507–519.
6 J. Wang, X. Zhuge and F. Zhuge, *Sci. Technol. Adv. Mater.*, 2021, **22**, 326–344.
7 A. S. Sokolov, H. Abbas, Y. Abbas and C. Choi, *J. Semicond.*, 2021, **42**, 013101.
8 W. Huang, X. Xia, C. Zhu, P. Steich, W. Quan, W. Mao, J. Yang, L. Chu and X. A. Li, *Nano-Micro Lett.*, 2021, **13**, 85–112.
9 Z. Shen, C. Zhao, Y. Qi, W. Xu, Y. Liu, I. Z. Mitrovic, L. Yang and C. Zhao, *Nanomaterials*, 2020, **10**, 1437.
10 J. Pei, L. Deng, S. Song, M. Zhao, Y. Zhang, S. Wu, G. Wang, Z. Zou, Z. Wu, W. He, F. Chen, N. Deng, S. W. Y. Wang, Y. Wu, Z. Yang, C. Ma, G. Li, W. Han, H. Li, H. Wu, R. Zhao, Y. Xie and L. Shi, *Nature*, 2019, **572**, 106–111.
11 Y. Li, Z. Wang, R. Midya, Q. Xi and J. J. Yang, *J. Phys. D: Appl. Phys.*, 2018, **51**, 503002.
12 C.-H. Hsu, Y.-S. Fan and P.-T. Liu, *Appl. Phys. Lett.*, 2013, **102**, 062905.
13 Z. Q. Wang, H. Y. Xu, X. H. Li, X. T. Zhang, Y. X. Liu and Y. C. Liu, *IEEE Electron Device Lett.*, 2011, **32**, 1442.
14 C. H. Kim, Y. H. Jang, H. J. Hwang, C. H. Song, Y. S. Yang and J. H. Cho, *Appl. Phys. Lett.*, 2010, **97**, 062109.
15 M.-C. Chen, T.-C. Chang, S.-Y. Huang, S.-C. Chen, C.-W. Hu, C.-T. Tsai and S. M. Sze, *Electrochem. Solid-State Lett.*, 2010, **13**, H191–H193.
16 F. Qin, Y. Zhang, H. Park, C. S. Kim, D. H. Lee, Z.-T. Jiang, J. Park, K. No, H. Park, H. W. Song and S. Lee, *Phys. Status Solidi RRL*, 2022, **16**, 1–11.
17 W. S. Choi, J. T. Jang, D. Kim, T. J. Yang, C. Kim, H. Kim and D. H. Kim, *Chaos, Solitons Fractals*, 2022, **156**, 111813.
18 H.-W. Choi, K.-W. Song, S.-H. Kim, K. T. Nguyen, S. B. Eadi, H.-M. Kwon and H.-D. Lee, *Sci. Rep.*, 2022, **12**, 1259.
19 S.-Y. Min and W.-J. Cho, *Nanomaterials*, 2021, **11**, 1081.
20 M. Pereira, J. Deuermeier, R. Nogueira, P. A. Carvalho, R. Martins, E. Fortunato and A. Kiazadeh, *Adv. Electron. Mater.*, 2020, **6**, 2000242.
21 J. T. Jang, G. Ahn, S.-J. Choi, D. M. Kim and D. H. Kim, *Electronics*, 2019, **8**, 1087.
22 H. Abbas, A. Ali, J. Jung, Q. Hu, M. R. Park, H. H. Lee, T.-S. Yoon and C. J. Kang, *Appl. Phys. Lett.*, 2019, **114**, 093503.
23 Y. Pei, B. Mai, X. Zhang, R. Hu, Y. Li, Z. Chen, B. Fan, J. Liang and G. Wang, *J. Electron. Mater.*, 2015, **44**, 645–650.
24 R. Kamal, P. Chandravanshi, D.-K. Choi and S. M. Bobade, *Curr. Appl. Phys.*, 2015, **15**, 648–653.
25 W. Hu, L. Zou, X. Chen, N. Qin, S. Li and D. Bao, *ACS Appl. Mater. Interfaces*, 2014, **6**, 5012–5017.
26 M.-S. Kim, Y. H. Hwang, S. Kim, Z. Guo, D.-I. Moon, J.-M. Choi, M.-L. Seol, B.-S. Bae and Y.-K. Choi, *Appl. Phys. Lett.*, 2012, **101**, 243503.
27 P. Ma, G. Liang, Y. Wang, Y. Li, Q. Xin, Y. Li and A. Song, *IEEE Trans. Electron Devices*, 2019, **66**, 2600–2605.
28 M. Asif and A. Kumar, *Mater. Today Electron.*, 2022, **1**, 100004.

29 S. K. Nandi, X. Liu, D. K. Venkatachalam and R. G. Elliman, *Phys. Rev. Appl.*, 2015, **4**, 064010.

30 C. Charpin-Nicolle, M. Bonvalot, R. Sommer, A. Persico, M. L. Cordeau, S. Belahcen, B. Eychenne, P. Blaise, S. Martinie, S. Bernasconi, E. Jalaguier and E. Nowak, *Microelectron. Eng.*, 2020, **221**, 111194.

31 Y. Ahn, H. W. Shin, T. H. Lee, W.-H. Kim and J. Y. Son, *Nanoscale*, 2018, **10**, 13443–13448.

32 R. Hu, X. Li, J. Tang, Y. Li, X. Zheng, B. Gao, H. Qian and H. Wu, *Adv. Electron. Mater.*, 2021, **8**, 2100827.

33 F. Widdascheck, M. Kothe, A. A. Hauke and G. Witte, *Appl. Surf. Sci.*, 2020, **507**, 145039.

34 F. Hajakbari, S. Rashvand and A. Hojabri, *J. Theor. Appl. Phys.*, 2019, **13**, 365–373.

35 P. Fuchs, *Appl. Surf. Sci.*, 2009, **256**, 1382–1390.

36 M. Quaas, O. Ivanova, C. A. Helm and H. Wulff, *Z. Kristallogr. Suppl.*, 2008, **27**, 295–302.

37 Z. Li, P. Beck, D. A. A. Ohlberg, D. R. Stewar and R. S. Williams, *Surf. Sci.*, 2003, **529**, 410–418.

38 M.-J. Lee, G.-S. Park, D. H. Seo, S. M. Kwon, H.-J. Lee, J.-S. Kim, M. Jung, C.-Y. You, H. Lee, H.-G. Kim, S.-B. Pang, S. Seo, H. Hwang and S. K. Park, *ACS Appl. Mater. Interfaces*, 2018, **10**, 29757–29765.

39 R. A. Martins, E. Carlos, J. Deuermeier, M. E. Pereira, R. Martins, E. Fortunato and A. Kiazadeh, *J. Mater. Chem. C*, 2022, **10**, 1991–1998.

40 H. Xie, J. Xu, G. Liu, L. Zhang and C. Dong, *Mater. Sci. Semicond. Process.*, 2017, **64**, 1–5.

41 T. T. Trinh, K. Jang, S. Velumani, V. A. Dao and J. Yi, *Mater. Sci. Semicond. Process.*, 2015, **38**, 50–56.

42 J. Raja, K. Jang, N. Balaji, S. Q. Hussain, S. Velumani, S. Chatterjee, T. Kim and J. Yi, *Mater. Sci. Semicond. Process.*, 2015, **37**, 129–134.

43 J. C. C. Fan and J. B. Goodenough, *J. Appl. Phys.*, 1977, **48**, 3524–3531.

44 K. Krishnan, S. M. Tauquir, S. Vijayaraghavan and R. Mohan, *RSC Adv.*, 2021, **11**, 23400–23408.

45 Q. Liu, H. Qin, J. A. Boscoboinik and G. Zhou, *Langmuir*, 2016, **32**, 11414–11421.

46 Q. Li, L. Qiu, X. Wei, B. Dai and H. Zeng, *Sci. Rep.*, 2016, **6**, 1–8.

47 C. Fei, H. Liu, X. Wang, D. Zhao and S. Wang, *J. Mater. Sci.: Mater. Electron.*, 2016, **27**, 8550–8558.

48 E. Ozensoy, J. Szanyi and C. H. F. Peden, *J. Phys. Chem. B*, 2005, **109**, 3431–3436.

49 J. T. Jang, J. Min, D. Kim, J. Park, S.-J. Choi, D. M. Kim, S. Cho and D. H. Kim, *Solid-State Electron.*, 2020, **166**, 107764.

50 H. J. Lee, D. Kim, W. S. Choi, C. Kim, S.-J. Choi, J.-H. Bae, D. M. Kim, S. Kim and D. H. Kim, *Mater. Sci. Semicond. Process.*, 2023, **153**, 107183.

51 M. E. Pereira, J. Deuermeier, P. Freitas, P. Barquinha, W. Zhang, R. Martins, E. Fortunato and A. Kiazadeh, *APL Mater.*, 2022, **10**, 1–10.

52 M. E. Pereira, J. Deuermeier, C. Figueiredo, Â. Santos, G. Carvalho, V. G. Tavares, R. Martins, E. Fortunato, P. Barquinha and A. Kiazadeh, *Adv. Electron. Mater.*, 2022, **8**, 2200642–2200652.

53 W. S. Choi, M. S. Song, H. Kim and D. H. Kim, *Micromachines*, 2022, **13**, 1–10.

54 W. S. Choi, D. Kim, T. J. Yang, I. Chae, C. Kim, H. Kim and D. H. Kim, *Chaos, Solitons Fractals*, 2022, **158**, 112106.

55 G. Carvalho, M. E. Pereira, C. Silva, J. Deuermeier, A. Kiazadeh and V. Tavares, *AIP Adv.*, 2022, **12**, 085017.

56 A. de Jamblinne de Meux, G. Pourtois, J. Genoe and P. Heremans, *Phys. Rev. Appl.*, 2018, **9**, 054039.

57 E. W. Lim and R. Ismail, *Electronics*, 2015, **4**, 586–613.

58 T. Kamiya, K. Nomura and H. Hosono, *Sci. Technol. Adv. Mater.*, 2010, **11**, 044305.

59 K. Ide, K. Nomura, H. Hosono and T. Kamiya, *Phys. Status Solidi A*, 2019, **216**, 1800372.

60 T. Kamiya and H. Hosono, *NPG Asia Mater.*, 2010, **2**, 15–22.

61 C.-C. Yen, A.-H. Tai, Y. C. Liu, T. L. Chen and C. H. Chou, *J. Electron Devices Soc.*, 2020, **8**, 540–544.

62 M. Mativenga, F. Haque, M. M. Billah and J. G. Um, *Sci. Rep.*, 2021, **11**, 1–12.

63 G. Li, A. Abliz, L. Xu, N. Andre, X. Liu, Y. Zeng, D. Flandre and L. Liao, *Appl. Phys. Lett.*, 2018, **112**, 253504.

64 H. Han, S. Jang, D. Kim, T. Kim, H. Cho, H. Shin and C. Choi, *Electronics*, 2022, **11**, 1–12.

65 F. Pan, S. Gao, C. Chen, C. Song and F. Zeng, *Mater. Sci. Eng., R*, 2014, **83**, 1–59.

66 V. Chakrapani, in *Encyclopedia of Applied Electrochemistry*, ed. K.-I. O. Gerhard Kreysa and R. F. Savinell, Springer, New York, NY, 2014, pp. 1882–1893.

67 W. Sun, B. Gao, M. Chi, Q. Xia, J. J. Yang, H. Qian and H. Wu, *Nat. Commun.*, 2019, **10**, 3453.

68 Z. Q. Wang, H. Y. Xu, H. L. Xing, H. Yu, Y. C. Liu and X. J. Zhu, *Adv. Funct. Mater.*, 2012, **22**, 2759–2765.

69 T. Chang, S.-H. Jo and W. Lu, *ACS Nano*, 2011, **5**, 7669–7676.

70 D. C. Rubin and A. E. Wenzel, *Psychol. Rev.*, 1996, **103**, 734–760.

71 B. Sturman, E. Podivilov and M. Gorkunov, *Phys. Rev. Lett.*, 2003, **91**, 176602–176605.